RSC Advances

ROYAL SOCIETY OF CHEMISTRY

www.rsc.org/advances

First principles investigation of NO_2 and SO_2 adsorption on γ-Al_2O_3 supported mono- and diatomic metal clusters

Zuleyha Artuc,[†] Hande Ustunel,[‡,§] and Daniele Toffoli[*,¶,§]

Micro and Nanotechnology Department, Middle East Technical University, 06800, Ankara, Turkey, Department of Physics, Middle East Technical University, 06800, Ankara, Turkey, and Department of Chemistry, Middle East Technical University, 06800, Ankara, Turkey

E-mail: dtoffoli@metu.edu.tr

Abstract

NO_x storage/reduction catalysts have been developed in the 1990's to minimize the emission of harmful NO and NO_2 gases as a result of lean burning in diesel engines. Sulfur poisoning of the catalyst occurs when SO_x (x=2-3) species present in the fuel react aggressively with both the storage and the precious metal redox components. In the present work, DFT calculations within the plane wave, pseudopotential GGA framework were performed to study NO_2 and SO_2 adsorption on mono and diatomic clusters of Pt and Rh supported on the γ-Al_2O_3 (100) surface. The most stable adsorption geometries for the clusters on the surface were identified and used as anchoring points for the adsorption of NO_2 and SO_2 molecules. Binding energies of a large number of NO_2 and SO_2 adsorption geometries were reported. In all cases where direct

*To whom correspondence should be addressed
[†]Micro and Nanotechnology Department, Middle East Technical University, 06800, Ankara, Turkey
[‡]Department of Physics, Middle East Technical University, 06800, Ankara, Turkey
[¶]Department of Chemistry, Middle East Technical University, 06800, Ankara, Turkey
[§]Micro and Nanotechnology Department, Middle East Technical University, 06800, Ankara, Turkey

comparison between NO_2 and SO_2 binding geometries was possible, NO_2 binding energies were observed to be larger than SO_2 binding energies, in some cases by more than 1 eV.

1 Introduction

Three-way catalytic converters (TWCs) have been successfully used for decades in conventional automobile engines for the elimination of pollutants. An important shortcoming, however, presents itself when TWCs are used in tandem with the more fuel-efficient lean-burn diesel engines. Optimized for stoichiometric fuel consumption, which corresponds approximately to 14.7:1 air-to-fuel ratio, TWCs fail to efficiently eliminate the harmful NO and NO_2 (NO_x) by-products under lean burning conditions of about a 22:1 air-to-fuel ratio. In 1994, Toyota developed a new class of catalysts that reduce the harmful NO and NO_2 gases to N_2 at the same time converting hydrocarbons to CO_2 and water under lean conditions.[1] Known generically as NO_x storage/reduction (NSR) catalysis, this novel process has enjoyed considerable success since its inception, and a large body of experimental[2–7] and theoretical[8–12] research has been devoted to its optimization. The common goal of this research effort is to meet the limits and regulations put forward by various environmental agencies around the world.[13]

A typical NO_x storage/reduction cycle takes place in two stages.[14,15] The NO and NO_2 species that are released as combustion by-products first react during a long, *lean* period with **the redox** component, **typically Pt**,[16–18] , which **oxidizes** most of the incoming NO into NO_2. The NO_x **(mostly NO_2)** species are then **trapped in** the storage component, BaO **in the typical NSR catalysts,** and stored as bulk and surface nitrites and nitrates. **During** a brief *fuel-rich* **period** follow**ing** the lean period, the stored nitrites and nitrates are **decomposed** and **NO_2 is reduced to N_2 on the surface of the precious metal, in the presence of reducing agents such as H_2, CO and hydrocarbons**. The redox and storage components are supported by a third component, which is often another oxide.

The most commonly used support material is γ-Al_2O_3 although many alternatives have been proposed over the years. The support component **whose main role is to efficiently disperse the precious metal and trapping component**, can actively participate in the cycle by means of controlling the acidity of the adsorbed species.[19] **Performance of NSR systems depends crucially upon the efficiency of each of the components as well as their mutual interactions which can affect in a complex way, either directly or indirectly the activity of the catalyst.[20] The use of model systems, as typically reported in the NSR literature, is therefore valuable in isolating specific trends as, for example, the interaction of the adsorbates with a specific component of the catalyst, beside being the only way in which complex systems such as the NSR catalyst, can be modelled by first principle quantum mechanical methods.**

One of the main deactivation mechanisms of NSR catalysts is sulfur poisoning,[21] which reduces the performance of both the precious metal and the storage component.[17,22–24] Oxides of sulfur (SO_x) exist in small but noticable quantities in fuel. Due to their higher affinity towards the storage and reduction components, SO_x species compete with NO_x for the same adsorption sites, binding much more strongly and blocking further NO_x adsorption. Theoretical and experimental studies indicate that transition metals show a high affinity towards all SO_x species especially under oxygen-rich conditions.[25] Even SO_2, the least reactive of the SO_x species,[25] is oxidized on the metal component very quickly and converted into the more agressive SO_3 and SO_4 species.[26] Several remedies have been suggested over the years against sulfur poisoning including alternative support materials,[19] and **the use of other precious metals such as Pd and Rh or metal alloys in place of Pt.**[27–29] In particular, small clusters of pure metals are expected to have increased activity. In a density functional theory (DFT) study Pan et al[30] showed that dimers of 3d-metals on a γ-Al_2O_3 support increase the activity of CO_2 by donating their charges.

Alloys have long been known to display superior qualities in comparison to their constituents for diverse purposes.[31–33] Tang and Trout found that the addition of Rh and Pd

to a clean Pt(111) surface significantly improved NO chemisorption.[27] In a recent study,[28] RhPt-containing catalysts were shown to improve NO_x reducibility without negatively affecting the storage capacity. Similarly, Bobadilla et al.[29] found that addition of Pd to a $Pt/Ba/CeO_2/Al_2O_3$ catalyst improves the initial NO oxidation due to the alloying effect.

In the present work, we use DFT to explore the sulfur tolerance of mono and diatomic Pt and Rh clusters supported on γ-Al_2O_3, by comparing the stability of adsorbed NO_2 and SO_2 species. We choose the γ-$Al_2O_3(100)$ surface, because it presents numerous distinct **adsorption** sites **as a result of its open structure.** We **start by** explor**ing** surface adsorption sites **for single Pt and Rh atoms** on γ-Al_2O_3, identify**ing** the most stable configurations. We **then** study the adsorption of a second Pt or Rh atom. Binding energies of NO_2 and SO_2 molecules **are then calculated both** on isolated and γ-Al_2O_3-supported monoatomic and diatomic clusters. A comparative discussion of the relative stabilities of the two adsorbates is then presented.

Our paper is organized as follows. In section 2, we describe our computational method. **A discussion of the results is** presented in section 3. Conclusions are reported in section 4.

2 Method

The calculations were performed using plane-wave pseudopotential density functional theory[34,35] within the gradient-corrected approximation (GGA). The Perdew-Becke-Ernzerhof[36] exchange-correlation functional as implemented in the Quantum-Espresso **distibution**[37] was used in all calculations. The open-source program XCrysDen[38] was used for visualization and to produce the figures. During BFGS geometry optimizations, a force threshold per atom of 0.025 eV/Å was used. Ultrasoft pseudopotentials[39] were used to model the interaction between nuclei and electrons, which allow an affordable kinetic energy cutoff of 35 Ryd and a density cutoff of 350 Ryd.

Despite **being** used in **a large number of** applications,[40–42] **the** bulk and surface

structures of γ-Al_2O_3 are still under debate.[43–47] Two models are proposed for the bulk structure of γ-Al_2O_3: a spinel-like structure with vacancies introduced in order to match the stoichiometry[48] and a nonspinel structure derived from boehmite.[44,49] Attempts to distinguish these two structures have been largely inconclusive due to their similar spectroscopic signatures. In this work, the nonspinel tetragonal model, illustrated in Figure 1, proposed by Krokidis and Digne has been used.[44,49] The conventional unit cell contains 16 Al and 24 O atoms; 3/4 of the Al atoms occupy penta-coordinated lattice sites while the remaining 1/4 are tetra-coordinated. In this work, the lattice constants of γ-Al_2O_3 were calculated through a variable-cell relaxation.[50] The calculated cell parameters ($a = 5.587$ Å, $b = 8.413$ Å, and $c = 8.009$ Å) are in very good agreement with previous results.[51]

The (100) surface of γ-Al_2O_3 was modeled using an asymmetric, eight-layer slab with no fixed layers. The surface energy was calculated to be 1.03 J/m^2, which compares favorably with the value of 0.97 J/m^2 quoted by Digne et al.[49] As a further test of the slab model used in the calculation, the surface energy was calculated for a sixteen-layer slab with no fixed layers and was found to be 1.06 J/m^2 confirming the accuracy of the eight-layer slab model. The 1×1 unit cell of the (100) surface of γ-Al_2O_3 consists of 5 distinct Al atoms and 6 distinct O atoms. In the following, we will refer to the surface Al atoms with numbers, and surface O atoms with letters. The labeling scheme was built upon the nomenclature introduced in the work by Deskins *et al*.[52] The (100) surface is illustrated in Figure 1. While Al atoms labeled 2 through 5 (Al(2)-Al(5)) are located at the surface level, Al(1) is a subsurface species. Clean surfaces and adsorption energies are studied in a 2×1 surface slab geometry with a k-point mesh of $2\times3\times1$. All calculations were spin-polarized.

Optimized geometries of NO_2 and SO_2 gas-phase molecules and isolated metal dimers were calculated in a large cubic simulation cell. NO_2 and SO_2 have a bent structure with bond lengths of 1.213 Å and 1.457 Å while the bond angles are 133.6° and 119.4° respectively. The calculated bond lengths of Pt_2, Rh_2 and Pt-Rh are 2.36 Å, 2.23 Å and 2.32 Å respectively while the bond energies per atom are 3.09 eV, 2.29 eV and 3.66 eV in good

agreement with previous results.[53,54] Pt_2, Rh_2 and Pt-Rh clusters all prefer high-spin states with magnetizations of 2.0 μ_B, 4.0 μ_B and 3.0 μ_B respectively.

Initial geometries for NO_2 and SO_2 adsorption on the isolated clusters closely mimick the adsorption modes observed on Pt(111).[55] Following geometry optimization, binding energies were calculated using the formula below:

$$E_B = E_{\text{cluster}} + E_{\text{ad}} - E_{\text{cluster+ad}}, \tag{1}$$

where $E_{\text{cluster+ad}}$, E_{cluster} and E_{ad} denote the total energy of the cluster with the adsorbed molecule, the energy of the isolated cluster and the energy of the gas-phase molecule. According to this definition, the binding energies of stable adsorbates are positive.

Charge density differences for NO_2 and SO_2 adsorption were calculated using

$$\Delta\rho(\vec{r}) = \rho_{\text{cluster+ad}}(\vec{r}) - \rho_{\text{cluster}}(\vec{r}) - \rho_{\text{ad}}(\vec{r}) \tag{2}$$

where $\rho_{\text{cluster+ad}}(\vec{r})$ is the charge density of the **full system** (cluster + adsorbate, NO_2 or SO_2). The charge density of the **isolated** cluster, $\rho_{\text{cluster}}(\vec{r})$, and that of the **isolated** $\mathbf{NO_2}$ **and** $\mathbf{SO_2}$ **molecules** $\rho_{ad}(\vec{r})$ were separately calculated in the simulation cell used for the cluster-adsorbate system.

Binding energies of single Rh or Pt **atoms adsorbed on the** $\gamma{-}Al_2O_3$ **(100) surface** were calculated using the following expression:

$$E_B = E_{\text{surf}} + E_{\text{M}} - E_{\text{surf+M}}, \tag{3}$$

where $E_{\text{surf+M}}$, E_{surf} and E_{M} **denotes, respectively,** the total energy of the surface with the adsorbed metal atom (M), the energy of the bare surface and the energy of the isolated metal atom. For the adsorption of the second metal **atom on the preadsorbed single metal atom, there are four possibilities, namely Pt-Pt, Rh-Rh, Rh-Pt, and Pt-**

Rh where for instance the notation Pt-Rh refers to the case in which Rh was the preadsorbed atom on the surface. A large-scale exploration of possible binding geometries yields some 100 configurations. **In this case** the binding energy is defined with respect to the surface with the first metal atom already adsorbed and is therefore calculated according to:

$$E_B = E_{\text{surf+M1}} + E_{\text{M2}} - E_{\text{surf+2M}}, \tag{4}$$

where $E_{\text{surf+2M}}$, $E_{\text{surf+M1}}$ and E_{M2} denote the total energy of the surface with the adsorbed diatomic cluster, the energy of the surface with the first metal atom, and the energy of the isolated second metal atom **respectively**. This method of calculating binding energies corresponds to an experimental scenario where the second metal atom in the diatomic cluster attaches to the first one as a result of surface diffusion. This is, in fact, a realistic assumption based on diffusion as a viable mechanism.[56,57] Finally, binding energies of NO_2 and SO_2 on $\gamma-Al_2O_3$ supported mono- and diatomic clusters were calculated with a simple generalization of Eq. (1). **Partial charges on selected atoms were computed using a Bader charge analysis.**[58]

3 Results and Discussion

3.1 Monoatomic and diatomic metal clusters supported on γ-Al_2O_3(100)

The adsorption of a single Pt atom on the γ-Al_2O_3(100) surface has previously been studied by Deskins et al.[52] **where** Pt atoms **were observed to preferentially adsorb at** bridging sites between O and neighboring Al atoms **with the exception of the adsorption configuration on Al(1) where a considerable downward motion of Pt towards the embedded Al atom was observed**. In the present work, the Pt atom was positioned at a large number of surface sites and was **subjected to geometry optimization.** Two of the six **stable** configurations identified in the present work can be directly compared to those

reported by Deskins et al., (see Table 1). In addition we identified new adsorption sites as a result of a larger set of initial starting configurations **explored in the present work** . However, the newly identified configurations differ only slightly in environment and binding energy from those already reported.[52]

For Pt, all adsorption configurations are displayed in Figure 2 and adsorption energies are reported in Table 1 **along with the distances between the metal atom and the surface. The metal-surface distance is taken to be the center-to-center vertical elevation of the metal with respect to a nearby, unperturbed penta-coordinated surface Al center.** Pt adsorbed on γ-Al_2O_3 displays rather small spin polarization. **T**he adsorption geometries fall into three categories, namely bridge (Figure 2(a,b)), **atop** (Figure 2(c)) and embedded (Figure 2(d-f)). The binding energies of bridge and **atop** configurations are very similar (**in the range** 1.60-1.81 eV) while those of the three embedded configurations are much larger (3.23-3.45 eV) as may be expected from the increased number of bonds and **shorter bond distances**. The uplifting of neighboring O atom in the embedded configurations noted by Deskins et al.[52] was also observed here as can be seen in the side view panels of Figure 2. **For all six configurations, there is a charge transfer from the surface to the Pt, in agreement with previous results** .[52] As a concrete example, the Bader charge on Pt for the most stable embedded adsorption configuration is -0.24 |e|.

Rh adsorbs with somewhat different binding geometries **on the γ-Al_2O_3 (100) surface**. The tendency of the Rh atom is to form bonds between two O(Al) and one Al(O) atoms. The binding geometries are displayed in Figure 3 and the binding energies are reported in Table 1. **Similarly to Pt, the minimum energy configurations for the Rh atom correspond to embedded geometries. However, for the embedded configurations, the Pt binding energies are higher by about 1 eV. This difference can be explained by observing that at variance with Pt,** the Rh atom tends to sit above the surface in the embedded configuration rather than being completely incorporated in the surface.

In fact, as seen in Table 1 **, the vertical Rh-surface distance is larger than the Pt-surface distance in the embedded configurations by about 0.20-0.35 Å. The remaining Rh binding configurations have similar binding energies to those of Pt.** The most stable configuration of a single Rh on the non-hydrated γ-Al_2O_3(100) surface, **calculated** by Shi et al.,[54] is similar to the most stable configuration identified in this work. **Their calculated binding energy (3.39 eV) also compares favorably with our result (3.07 eV). Similarly to single Pt adsorption, the charge transfer is from the surface to the Rh atom, in agreement with Shi et al.[54] For the most stable adsorption configuration, the amount of the charge transfer is -0.09 |e|.**

Following the identification of the **most stable** adsorption sites of the first metal atom (Pt or Rh), a second metal atom (Pt or Rh) is introduced. This results in a very large number of possible adsorption geometries for the dimer. The adsorption geometries of the Pt_2, Rh_2, Pt-Rh and Rh-Pt clusters, together with the binding energies of the second atom calculated using Eq. (4) are displayed in Figures 4-7. Overall, the binding energy of the second metal to the first is significantly larger than the binding energy of the first metal to the surface. **Moreover**, we observe a further small charge transfer from the surface to the cluster, upon adsorption of the second metal atom. As a concrete example, the total charge on the Pt_2 cluster displayed in Figure 4(d) is about -0.40|e|.

The binding energies of the second metal are consistent with the bond energies for the isolated metal clusters, that are 3.09 eV, 2.29 eV and 3.66 eV for Pt_2, Rh_2 and Pt-Rh respectively, the only exception **being** when the first metal atom is embedded into the surface. In this case, the binding energy of the second metal is consistently lower. **This can be rationalized by the formation of two strong Pt-O and Rh-O bonds in the embedded configurations at variance with other configurations.**

3.2 NO_2 and SO_2 adsorption on isolated diatomic clusters

In order to gain insight into the adsorbate-cluster interaction and to characterize the effect of the support, we **first studied** the adsorption of NO_2 and SO_2 molecules on isolated Pt_2, Rh_2 and PtRh diatomic clusters. Binding geometries **of NO_2 and SO_2** on isolated Pt_2 clusters are reported in Figure 8. Binding geometries of NO_2 and SO_2 on isolated Rh_2 and Pt-Rh clusters are very similar to those found in the Pt_2 case and are not reported in the Figure. **Calculated binding energies, bond angles and Bader charges for NO_2 and SO_2 adsorption on the isolated clusters are reported in** Table 2 and Table 3 respectively. **Partial density of states (PDOS) plots for all NO_2 and SO_2 binding geometries are also included in** Figure 8 **along with PDOS plots for the isolated Pt_2 cluster, gas phase NO_2 and gas phase SO_2.** Three **different adsorption** geometries were previously identified by Getman and Schneider[55] on the Pt(111) surface[19,55] for the 1/16 NO_2 surface coverage, namely O–O bridge, N–O bridge (μ-N,O nitrito), and monodentate (nitro), with binding energies of 1.25 eV, 1.35 eV, and 1.24 eV respectively. **We observe rather similar adsorption configurations on the isolated metal clusters, as can be seen in Figure** 8. **On the other hand, SO_2 displays two binding geometries on pristine Pt(111) surface:**[25] an *S-down* configuration, a combination of monodentate and S-O bridge geometries, and a *flat* configuration where the plane of the SO_2 molecule is parallel to the Pt surface. **In the present work, we have identified three** SO_2 adsorption geometries: S-O bridge, O-O-bridge, and S-down monodentate (Figure 8), similar to the NO_2 adsorption geometries discussed above.

From the inspection of the results reported in Table 2 **several observations can be made. The NO_2 binding energies on Pt_2 are overall larger in comparison to the bare Pt(111) surface. The minimum-energy configuration found in this work, denoted here as "monodentate", is very similar to that reported by Xu et al.**[59] **In the case of Rh_2, the most stable configuration is instead the N–O bridge, and we observe that the NO_2–Rh_2 interaction is somewhat stronger compared**

to Pt_2. The minimum-energy configurations for NO_2 adsorption on Pt_2 and the bimetallic Pt-Rh system have instead comparable binding energy.

From the comparison of NO_2 and SO_2 binding energies, which are reported in Table 3, we conclude that SO_2 binding energies are generally significantly smaller. The binding energy difference between NO_2 and SO_2 is particularly pronounced for the O-O bridge configurations, with values as large as or more than 1 eV. Moreover, for SO_2 adsorption the minimum-energy configuration is the monodentate in the case of Pt_2, while the S–O bridge configuration is the preferred one in the case of Rh_2 and the Pt-Rh bimetallic system.

For both NO_2 and SO_2, electron charge transfers are from the cluster to the molecule and are generally large in the case of NO_2. The reduction of the NO_2 molecule upon adsorption is reflected by the lenghtening of the N–O bonds, and the decrease of the O–N–O angle from the value of 133.6°, characteristic of the gas-phase molecule, toward the value of 115°, characteristic of the nitrite anion. The bond angle reduction is particularly pronounced for the bridge N-O and bridge O-O adsorption geometries. For SO_2, the extent of the reduction of the O–S–O angle upon adsorption is not as pronounced, although invariably rather large for the S-O and O-O adsorption configurations. A donation-backdonation mechanism described by Happel et al.[25] can play a role in the interaction of NO_2 and SO_2 with the metallic clusters. This mechanism is illustrated in Figure 9 for both NO_2 and SO_2 O–O bridge adsorption mode. From the charge density difference plots for NO_2 and SO_2 adsorption on Pt_2, we observe that charge is displaced from the Pt d_{z^2} orbitals to the LUMO of the molecule. This charge transfer is accompanied by a backdonation from the HOMO of the molecule to the Pt d_{xz} and d_{yz} orbitals of the Pt atoms.

Additional information about the bonding of NO_2 and SO_2 on the isolated metal clusters, can be gained from the inspection of the results of the PDOS

analysis, which is reported in Figure 8 for Pt_2 isolated cluster. In the case of NO_2 adsorption, the higher binding energy of the monodentate and N-O bridge configurations compared to the O-O bridge can be related to the larger overlap, in the region between -5 eV and the Fermi energy, between the O-p derived states, which become dominant in the energy range of -5 to -2 eV, and the d-states of the metal. The O p-derived states are instead strongly localized around -5 eV in the case of the O-O bridge NO_2 adsorption geometry. Moreover, in the same energy range, the intensity of the N p-derived states is very low for both monodentate and N-O bridge configurations compared to the O-O bridge, indicating the presence of a larger partial positive charge on the N atom for the strongly bound configurations compared to the O-O bridge one. Similar arguments can be made to explain the extra-stability of the monodentate adsorption configuration of SO_2.

Another manifestation of the strong NO_2 interaction with the metallic clusters is the reduction of the NO_2 and cluster magnetic moments upon adsorption. The magnetic moment of the isolated molecule, which is 1.00 μ_B due to the unpaired electron, is reduced to nearly zero upon adsorption. This is accompanied by a similar decrease of the magnetic moment of the clusters. For instance, in the case of the N-O bridge NO_2 adsorption configuration on the Rh_2 cluster, the magnetic moment of Rh_2 decreases from 4.00 μ_B to 1.27 μ_B. A similar decrease in the cluster magnetization is observed for SO_2 adsorption.

3.3 NO_2 and SO_2 adsorption on γ-Al_2O_3-supported mono- and bi-metallic clusters

The binding energies of NO_2 and SO_2 **for** a large number of adsorption configurations have been summarized in Figure 10 **in the form of two scatter plots**. The upper panel of Figure 10 displays NO_2 and SO_2 binding energies on single Pt and Rh atoms preadsorbed on the γ-Al_2O_3(100) surface, organized according to both binding geometry and metal atom

type. The lower panel of Figure 10 reports instead NO_2 and SO_2 adsorption energies on the supported diatomic clusters **and is organized in a similar manner**. In the plot, no distinction was made between Pt-Rh and Rh-Pt clusters.

Focusing for the moment on the supported metal atoms, we observe that the NO_2 binding energies are, in almost all cases, significantly larger than those for the corresponding geometries on bare Pt(111).[55] For the O-O-bridge and N-O-bridge configurations, this increase in binding energies may originate **either from the interaction between the surface Al atom and the free O atom of the NO_2 molecule or from the interaction between the molecule and the metal atom.** The strength of the interaction between the NO_2 and the surface Al atom can be qualitatively assessed by taking into account the rather low NO_2 and NO_3 binding energies on the bare $Al_2O_3(100)$ surface calculated by Mei et al[60] where the Al–ONO bond distance for a range of binding configurations is around 2.00 Å indicating a weak bond. In the present work, for supported metal atoms the Al–ONO bond lengths for the O-O-bridge and N-O-bridge geometries are in the range of 1.88-2.00 Å. This represents, about 5–6% reduction in the bond length compared to the pristine $Al_2O_3(100)$ surface, indicating a somewhat stronger interaction **between the Al atoms of the surface and the adsorbate**. **It appears then** that the precious metal-NO_2 interaction is mostly responsible for the increase in NO_2 stability on the supported metal atoms compared to the pristine metal surface. **However, the interaction of the adsorbate with the surface Al atom should not be overlooked.** In fact in a large number of geometry optimizations that begin with an initial configuration on the monodentate geometry, the NO_2 molecule was observed to eventually tilt towards the surface in favor of the N-O-bridge geometry.

Nearly all the NO_2 adsorption energies fall in the range 2.0-3.7 eV. **The lower adsorption energies in this range correspond to NO_2 molecules attached to embedded metal atoms, which can be explained by the relatively stronger interaction of the preadsorbed atom with the alumina surface. It is also worth to note that on γ-Al_2O_3 supported Pt atom, SO_2 binds significant more strongly than NO_2 in**

the monodentate adsorption configuration. This is an exception to a well defined trend where NO_2 is seen to adsorb more strongly than SO_2.

The NO_2 and SO_2 binding energies on supported diatomic clusters Pt_2, Rh_2, Pt-Rh and Rh-Pt are displayed in the bottom panel of Figure 10. The same three geometries found in the case of isolated clusters, (monodentate, N(S)-O bridge, O-O bridge) are observed also in this case. NO_2 tends to adsorb with higher binding energies on supported Rh_2 as compared to the other diatomic clusters, while NO_2 adsorption energies on Pt-Rh clusters are lower than **those calculated for the supported Pt_2 clusters. Moreover, for all supported metal clusters, the monodentate adsorption configuration is generally characterized by lower binding energies compared to the other two adsorption modes.**

The largest SO_2 binding energies are found on supported clusters with at least one Rh atom. All molecules adsorbed in the monodentate geometry have O-S-O angles above 116°, consistent with the findings of Happel et al.[25] **in the case of SO_2 adsorption on the pristine Pt(111) surface**. The S-O bridge configuration on the other hand **is characterized by lower** O-S-O angles (> 109°), **and the adsorption geometry is rather similar to the flat configuration, characterized for SO_2 adsorption on the Pt(111) surface.**[25] **In fact, in all S-down configurations identified in the present work, there is a tendency of the molecule to reorient itself parallel to the surface.**

Aside from these general trends, direct comparison of NO_2 and SO_2 binding energies for similar adsorption configurations was possible only for a limited number of systems. In Figure 11 and Figure 12, we report representative examples **along with the corresponding PDOS analysis.** Selected geometrical parameters are also listed in Table 4 for all geometries displayed in Figure 11 and Figure 12.

The O-O bridge and N/S-O bridge configurations for supported atomic Rh are presented in Figure 11. **For both adsorption configurations, the NO_2 binding energy is about 1 eV larger than that of SO_2 while the O–N–O bond angle is reduced and the**

bonds lengthened with respect to the gas phase values as a result of a charge transfer from the surface to the molecule. The O-S-O bond angle is similarly reduced along with an elongation of the bonds. **For both NO_2 and SO_2, the minimum energy configuration is the N(S)-O bridge. The extra stability of the N-O bridge over the O-O bridge configuration (about 0.8 eV), can be rationalized on the basis of the PDOS analysis, by the increased overlap between the metal d-states and the NO_2 O p-derived states (in the range -5 – -1 eV). The extra stability of the N-O bridge configuration can also be related to the stronger interaction between the NO_2 molecular orbitals (formed as linear combination of O-2p and N-2p orbitals) and Al derived states in the region around 8 eV below the Fermi energy. Similar observations can account for the extra stability of the S-O bridge configuration over the O-O bridge in the case of SO_2 adsorption.**

In Figure 12, we display a selection of NO_2 and SO_2 binding geometries with corresponding binding energies on supported diatomic clusters. The values quoted in parantheses in Figure 12 are binding energies for the corresponding adsorption geometries on the isolated clusters. Overall, NO_2 binding energies are observed to be larger than SO_2 binding energies by up to about 1 eV, in line with the general trend identified in this work, and clearly displayed in Figure 10. **The overall increase in the binding energies for both NO_2 and SO_2 on the supported clusters with respect to the isolated clusters clearly suggests that a surface mediated mechanism is active.**

From an inspection of Figure 12, **the following conclusions can be drawn. In the case of the monodentate adsorption configurations on the Pt_2 and the bimetallic supported cluster, we observe an extra stabilization of the SO_2 adsorbate, compared to NO_2, which is more pronounced for supported PtRh. By comparing the NO_2 and SO_2 binding energies for the N(S)-O bridge configurations on the supported clusters, we see that the effect of the γ-Al_2O_3 support is to strongly enhance the binding energies of both adsorbates. The effect of**

the support is however stronger in the case of the supported Pt_2 cluster (with an increase of binding energy by as large as 2 eV), compared to the bimetallic cluster. From the PDOS analysis we observe that in the case of supported Pt_2 the contribution of the metal d states extend in a wider energy region below the Fermi energy, when compared to the energy span of the d states in the bimetallic cluster, indicating a stronger interaction with both the surface and the adsorbate derived states.

Turning our attention on the O-O bridge geometry, we conclude that the effect of the support is to stabilize both adsorbates to roughly the same extent. In fact, in going from the isolated to the supported PtRh system, the adsorption energies for both NO_2 and SO_2 increases by about 1.5 eV, while on supported Rh_2, the increase in binding energy is 1 eV and 1.3 eV for NO_2 and SO_2 respectively.

An inspection of the results reported in Table 4 reveals that compared to the isolated clusters, the support enhances the amount of charge transfer to NO_2 upon adsorption. This last observation is corroborated by the further reduction of the O–N–O bond angle and the lengthening of the N–O bond distances induced by the support. Similar remarks apply, to a lesser extent, to SO_2. In addition, the larger binding energy of both adsorbates on the supported metal clusters is in line with the fact that the adsorption of NO_2 and SO_2 on the supported clusters, has little or no effect on the metal-metal distances of the preadorbed clusters, at variance with the isolated clusters.

4 Conclusion

In the present work, DFT calculations within the plane wave, pseudopotential GGA framework were performed to study NO_2 and SO_2 adsorption on mono and diatomic clusters of Pt and Rh supported on a γ-Al_2O_3 (100) surface. The defect-free non-spinel model for γ-Al_2O_3

was used. Several stable binding geometries were identified for single Pt and Rh atoms on the surface, and the results compared favorably with previous works. A second atom was subsequently adsorbed to form diatomic clusters (Pt_2, Rh_2 and PtRh). The binding energy of the second metal atom to the first was found to be in the range of 2-3 eV in line with the calculated metallic bond strength in isolated diatomic clusters.

NO_2 and SO_2 adsorption properties on isolated Pt_2, Rh_2 and PtRh clusters were studied and three binding geometries were identified. Overall, NO_2 and SO_2 adsorption energies on isolated diatomic clusters were found to be larger than those corresponding to pristine Pt surfaces reported in the literature. Moreover, for all clusters, NO_2 always binds much more strongly than SO_2.

Binding energies of a large number of NO_2 and SO_2 adsorption geometries on γ-Al_2O_3 supported diatomic clusters were reported. In a small subset of the geometries studied, direct comparison between NO_2 and SO_2 binding was possible. In all of these cases, NO_2 binding energies were larger than SO_2 binding energies, in some cases by 1 eV. While the differences between NO_2 and SO_2 binding energies were similar to those for isolated diatomic clusters, all binding energies were found to be larger for supported clusters than isolated clusters pointing toward an active role of the support.

Acknowledgement

This work was financially supported by TÜBITAK (Science and Technological Council of Turkey) Grant No. 108T706. We gratefully acknowledge the computational resources provided by the National Center of Academic Network and Information (TÜBITAK ULAKBIM) and the National Center for High Performance Computing (UHEM) Grant No. 10922010.

References

(1) Matsumoto, S.; Yokota, K.; Doi, H.; Kimura, M.; Sekizawa, K.; Kasahara, S. *Catalysis Today* **1994**, *22*, 127 – 146.

(2) Kwak, J.; Kim, D.; Szailer, T.; Peden, C.; Szanyi, J. *Catalysis Letters* **2006**, *111*, 119–126.

(3) Su, Y.; Kabin, K. S.; Harold, M. P.; Amiridis, M. D. *App Catal B* **2007**, *71*, 207.

(4) Piacentini, M.; Maciejewski, M.; Baiker, A. *Applied Catalysis B: Environmental* **2007**, *72*, 105 – 117.

(5) Kim, J.-G.; Lee, H.-M.; Lee, M.-J.; Lee, J.-H.; Kim, J.-G.; Jeon, J.-Y.; Jeong, S.-K.; Yoo, S.-J.; Kim, S.-S. *Journal of Industrial and Engineering Chemistry* **2008**, *14*, 841 – 846.

(6) Sakamoto, Y.; Matsunaga, S.; Okumura, K.; Kayama, T.; Yamazaki, K.; Takahashi, N.; Tanaka, T.; Kizaki, Y.; Motohiro, T.; Shinjoh, H. *Chemical Engineering Science* **2008**, *63*, 5028 – 5034.

(7) Kim, D. H.; Chin, Y.-H.; Muntean, G. G.; Yezerets, A.; Currier, N. W.; Epling, W. S.; Chen, H.-Y.; Hess, H.; Peden, C. H. F. *Industrial and Engineering Chemistry Research* **2006**, *45*, 8815–8821.

(8) Jelic, J.; Meyer, R. J. *Catalysis Today* **2008**, *136*, 76 – 83.

(9) Cheng, L.; Ge, Q. *The Journal of Physical Chemistry C* **2008**, *112*, 16924–16931.

(10) Kwak, J. H.; Mei, D.; Yi, C.-W.; Kim, D. H.; Peden, C. H.; Allard, L. F.; Szanyi, J. *Journal of Catalysis* **2009**, *261*, 17 – 22.

(11) Liu, Z.; Ma, L.; Junaid, A. S. M. *The Journal of Physical Chemistry C* **2010**, *114*, 4445–4450.

(12) Mei, D.; Kwak, J. H.; Szanyi, J.; Ge, Q.; Peden, C. H. *Catalysis Today* **2010**, *151*, 304 – 313.

(13) Vestreng, V.; Ntziachristos, L.; Semb, A.; Reis, S.; Isaksen, I. S. A.; Tarrasón, L. *Atmospheric Chemistry and Physics* **2009**, *9*, 1503–1520.

(14) Epling, W. S.; Campbell, L. E.; Yezerets, A.; Currier, N. W.; Parks, J. E. *Catalysis Reviews* **2004**, *46*, 163–245.

(15) Roy, S.; Baiker, A. *Chemical Reviews* **2009**, *109*, 4054–4091.

(16) Lietti, L. *Journal of Catalysis* **2001**, *204*, 175–191.

(17) Pereda-Ayo, B. n.; Botas-Echevarría, J. a.; González-Casablanca, J.; González-Marcos, M. P.; González-Velasco, J. R. *Catalysis Today* **2013**, *216*, 50–56.

(18) Shakya, B. M.; Harold, M. P.; Balakotaiah, V. *Catalysis Today* **2012**, *184*, 27–42.

(19) Hummatov, R.; Gulseren, O.; Ozensoy, E.; Toffoli, D.; Ustunel, H. *The Journal of Physical Chemistry C* **2012**, *116*, 6191–6199.

(20) Liu, G.; Gao, P.-X. *Catal. Sci. Technol.* **2011**, *1*, 552–568.

(21) Tanaka, T.; Amano, K.; Dohmae, K.; Takahashi, N.; Shinjoh, H. *Applied Catalysis A: General* **2013**, *455*, 16–24.

(22) Büchel, R.; Pratsinis, S. E.; Baiker, A. *Applied catalysis. B, Environmental* **2012**, *113-114*, 160–171.

(23) Matsumoto, S.; Ikeda, Y.; Suzuki, H.; Ogai, M.; Miyoshi, N. *Applied Catalysis B: Environmental* **2000**, *25*, 115–124.

(24) Rohr, F.; Peter, S.; Lox, E.; Kögel, M.; Sassi, a.; Juste, L.; Rigaudeau, C.; Belot, G.; Gélin, P.; Primet, M. *Applied Catalysis B: Environmental* **2005**, *56*, 201–212.

(25) Happel, M.; Luckas, N.; Vin, F.; Sobota, M.; Laurin, M.; Görling, J., Libuda *The Journal of Physical Chemistry. C* **2011**, *115*, 479–491.

(26) Miyoshi, N.; Matsumoto, S. *Sci Tech Catal* **1998**, 245.

(27) Tang, H.; Trout, B. L. *The Journal of Physical Chemistry. B* **2005**, *109*, 17630–4.

(28) Andonova, S.; Marchionni, V.; Borelli, M.; Nedyalkova, R.; Lietti, L.; Olsson, L. *Applied Catalysis B: Environmental* **2013**, *132-133*, 266–281.

(29) Bobadilla, L. F.; Marie, O.; Bazin, P.; Daturi, M. *Catalysis Today* **2013**, *205*, 24–33.

(30) Pan, Y.-x.; Liu, C.-j.; Wiltowski, T. S.; Ge, Q. *Catalysis Today* **2009**, *147*, 68–76.

(31) Lee, K.; Song, C.; Janik, M. J. *Applied Catalysis A: General* **2010**, *389*, 122 – 130.

(32) Lee, K.; Song, C.; Janik, M. J. *Langmuir : the ACS journal of surfaces and colloids* **2012**, *28*, 5660–8.

(33) Li, J.; Wu, G.; Guan, N.; Li, L. *Catalysis Communications* **2012**, *24*, 38–43.

(34) Hohenberg, P.; Kohn, W. *Phys. Rev.* **1964**, *136*, B864–B871.

(35) Kohn, W.; Sham, L. J. *Phys. Rev.* **1965**, *140*, A1133–A1138.

(36) Perdew, J. P.; Burke, K.; Ernzerhof, M. *Phys. Rev. Lett.* **1996**, *77*, 3865–3868.

(37) Giannozzi, P. et al. *Journal of Physics: Condensed Matter* **2009**, *21*, 395502.

(38) Kokalj, A. *Computational Materials Science* **2003**, *28*, 155 – 168.

(39) Vanderbilt, D. *Phys. Rev. B* **1990**, *41*, 7892–7895.

(40) Baranowska, K.; Okal, J.; Miniajluk, N. *Catalysis Letters* **2013**, *144*, 447–459.

(41) Trueba, M.; Trasatti, S. P. *European Journal of Inorganic Chemistry* **2005**, *2005*, 3393–3403.

(42) Miranda, B.; Chimentão, R.; Santos, J.; Gispert-Guirado, F.; Llorca, J.; Medina, F.; Bonillo, F. L.; Sueiras, J. *Applied Catalysis B: Environmental* **2014**, *147*, 464–480.

(43) Ching, W.; Ouyang, L.; Rulis, P.; Yao, H. *Physical Review B* **2008**, *78*, 014106.

(44) Krokidis, X.; Raybaud, P.; Gobichon, A.-E.; Rebours, B.; Euzen, P.; Toulhoat, H. *The Journal of Physical Chemistry B* **2001**, *105*, 5121–5130.

(45) Liu, X. *Journal of Physical Chemistry C* **2008**, *112*, 5066–5073.

(46) Ouyang, C.; Šljivančanin, v.; Baldereschi, A. *Physical Review B* **2009**, *79*, 235410.

(47) Paglia, G.; Buckley, C.; Rohl, A.; Hunter, B.; Hart, R.; Hanna, J.; Byrne, L. *Physical Review B* **2003**, *68*, 144110.

(48) Pinto, H.; Nieminen, R.; Elliott, S. *Physical Review B* **2004**, *70*, 125402.

(49) Digne, M.; Sautet, P.; Raybaud, P.; Euzen, P.; Toulhoat, H. *Journal of Catalysis* **2004**, *226*, 54–68.

(50) Wentzcovitch, R. M.; Martins, J. L.; Price, G. D. *Phys. Rev. Lett.* **1993**, *70*, 3947–3950.

(51) Ferreira, A. R.; Martins, M. J.; Konstantinova, E.; Capaz, R. B.; Souza, W. F.; Chiaro, S. S. X.; Leitão, A. a. *Journal of Solid State Chemistry* **2011**, *184*, 1105–1111.

(52) Deskins, N. A.; Mei, D.; Dupuis, M. *Surface Science* **2009**, *603*, 2793 – 2807.

(53) Yang, S. H.; Drabold, D. A.; Adams, J. B.; Ordej, P. *J. Phys.: Condens. Matter* **1997**, *9*, L39–L45.

(54) Shi, X.-R.; Sholl, D. S. *The Journal of Physical Chemistry C* **2012**, *116*, 10623–10631.

(55) Getman, R. B.; Schneider, W. F. *The Journal of Physical Chemistry C* **2007**, *111*, 389–397.

(56) Zhou, Y.; Muhich, C. L.; Neltner, B. T.; Weimer, A. W.; Musgrave, C. B. *The Journal of Physical Chemistry C* **2012**, *116*, 12114–12123.

(57) Deák, R.; Néda, Z. *Physica Status Solidi (b)* **2012**, *249*, 1709–1716.

(58) Henkelman, G.; Arnaldsson, A.; Jónsson, H. *Computational Materials Science* **2006**, *36*, 354–360.

(59) Xu, Y.; Getman, R. B.; Shelton, W. A.; Schneider, W. F. *Phys. Chem. Chem. Phys.* **2008**, *10*, 6009–6018.

(60) Mei, D.; Ge, Q.; Szanyi, J.; Peden, C. H. F. *The Journal of Physical Chemistry C* **2009**, *113*, 7779–7789.

Table 1: Binding sites, corresponding binding energies (B.E.) in eV and vertical surface-metal distances in Å of Pt and Rh on the γ-Al_2O_3 (100) surface. Values in parantheses are taken from Ref.[52]

Pt			Rh		
Site	B. E.	d	Site	B. E.	d
Al(5)-O(A)	1.81	1.98	Al(1)-O(A)-Al(5)	2.33	1.29
Al(2)-O(C)-Al(4)	1.60	2.00	Al(2)-O(A)-Al(5)	1.54	2.11
Al(2)-O(A)-Al(5)	1.63 (1.70)	2.17	O(A)-Al(1)-O(C)-Al(2)	2.33	1.30
O(C)-Al(3)-O(D)	3.45	0.82	Al(2)-Al(4)	1.82	1.16
O(E)-Al(3)-O(F)	3.35 (3.50)	0.96	O(C)-Al(3)-O(D)	3.07	1.17
O(A)-Al(2)-O(C)	3.23	0.95			

Table 2: NO_2 geometry and Bader charge (a.u.), and binding energies of NO_2 on Pt_2, Rh_2 and Pt-Rh unsupported clusters. The variation of the metal-metal distance (Δd) upon NO_2 adsorption is also reported. Bond angles are in degrees and bond distances in Å.

		∠(O-N-O)	N–O	Bader charge	Δd	E_B [eV]
	Mono	129.8	1.21/1.27	-0.32	0.03	2.02
Pt_2	N-O	123.1	1.22/1.29	-0.41	0.17	1.71
	O-O	121.1	1.27/1.27	-0.42	0.19	1.43
Rh_2	N-O	119.8	1.30/1.40	-0.61	0.16	2.44
	O-O	117.9	1.27/1.27	-0.59	0.16	2.17
	Mono (Pt-N)	126.4	1.24/1.24	-0.42	0.18	1.73
	Mono (Rh-N)	129.2	1.28/1.21	-0.39	0.0	2.05
Pt-Rh	N-O (Pt-N)	122.7	1.22/1.29	-0.48	0.25	1.92
	N-O (Rh-N)	120.2	1.22/1.33	-0.53	0.15	1.82
	O-O	120.0	1.28/1.25	-0.50	0.19	1.64

Table 3: SO_2 geometry and Bader charge (a.u.), and binding energies of SO_2 on Pt_2, Rh_2 and Pt-Rh unsupported clusters. The variation of the metal-metal distance (Δd) upon SO_2 adsorption is also reported. Bond angles are in degrees and bond distances in Å.

		∠(O-S-O)	S–O	Bader charge	Δd	E_B[eV]
	Mono	119.0	1.46/1.46	-0.15	0.05	1.44
Pt_2	S-O	114.5	1.48/1.63	-0.40	0.17	0.63
	O-O	110.0	1.53/1.53	-0.38	0.13	0.21
Rh_2	S-O	111.6	1.48/1.60	-0.56	0.16	1.91
	O-O	108.8	1.55/1.55	-0.59	0.16	0.91
	Mono(Pt-S)	115.4	1.45/1.44	-0.01	0.06	0.51
	Mono (Rh-S)	119.2	1.46/1.46	-0.22	0.03	1.19
Pt-Rh	S-O (Pt-S)	111.8	1.48/1.61	-0.48	0.18	1.66
	S-O (Rh-S)	112.3	1.49/1.63	-0.52	0.20	1.37
	O-O	110.2	1.54/1.54	-0.47	0.15	0.48

Table 4: NO_2 and SO_2 geometries and Bader charges (a.u.), for the adsorption geometries displayed in Figure 11 and Figure 12. The variation of the metal-metal distance (Δd) upon NO_2 and SO_2 adsorption is also reported. Bond angles are in degrees and bond distances in Å.

Figure	NO_2				SO_2			
	∠(O-N-O)	N-O (Å)	Bader charge	Δd (Å)	∠(O-S-O)	S-O (Å)	Bader charge	Δd (Å)
11(a,b)	118.17	1.28, 1.27	-0.45	—	111.89	1.54, 1.53	-0.46	—
11(c,d)	118.83	1.31, 1.23	-0.45	—	111.65	1.52, 1.46	-0.09	—
12(a,b)	117.75	1.35, 1.22	-0.19	-0.01	118.12	1.46, 1.46	0.31	0.00
12(c,d)	127.18	1.30, 1.22	-0.37	0.00	116.94	1.47, 1.47	-0.03	0.04
12(e,f)	117.45	1.34, 1.22	-0.20	0.00	111.61	1.59, 1.48	-0.30	-0.08
12(g,h)	119.34	1.22, 1.32	-0.32	0.08	112.00	1.48, 1.58	-0.17	0.09
12(i,j)	116.54	1.28, 1.30	-0.33	0.01	110.20	1.57, 1.55	-0.33	0.07
12(k,l)	116.18	1.29, 1.30	-0.56	-0.08	113.96	1.56, 1.56	-0.48	-0.06

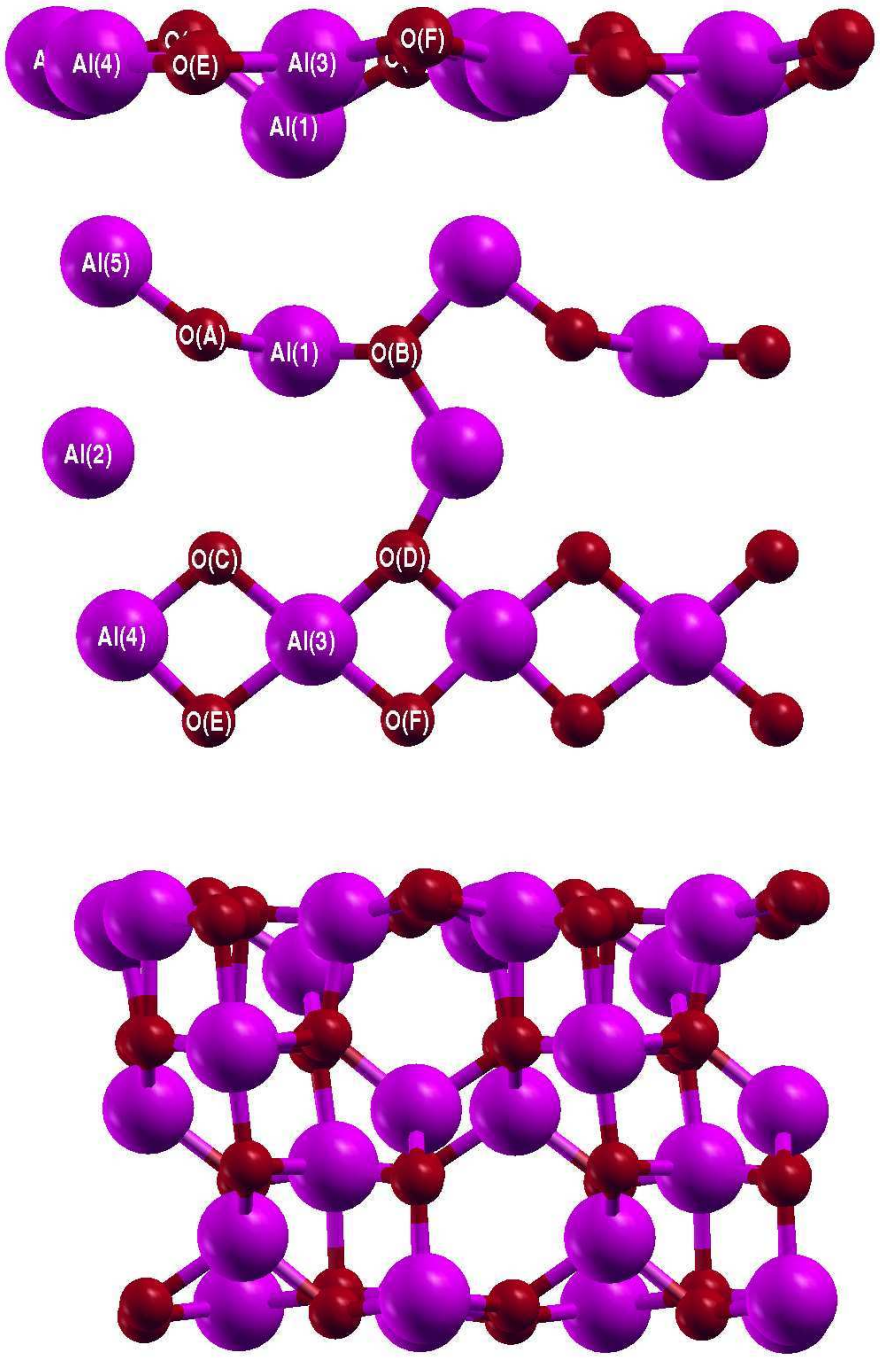

Figure 1: Upper panel: The top layer of the 2×1 γ-Al_2O_3 simulation cell used in this work displayed to reveal the embedded Al atom. Central panel: Labeling scheme used for surface Al and O atoms. Labels are built upon those used in the work of Deskins et al.[52] Lower panel: 2×1 simulation cell used in this work.

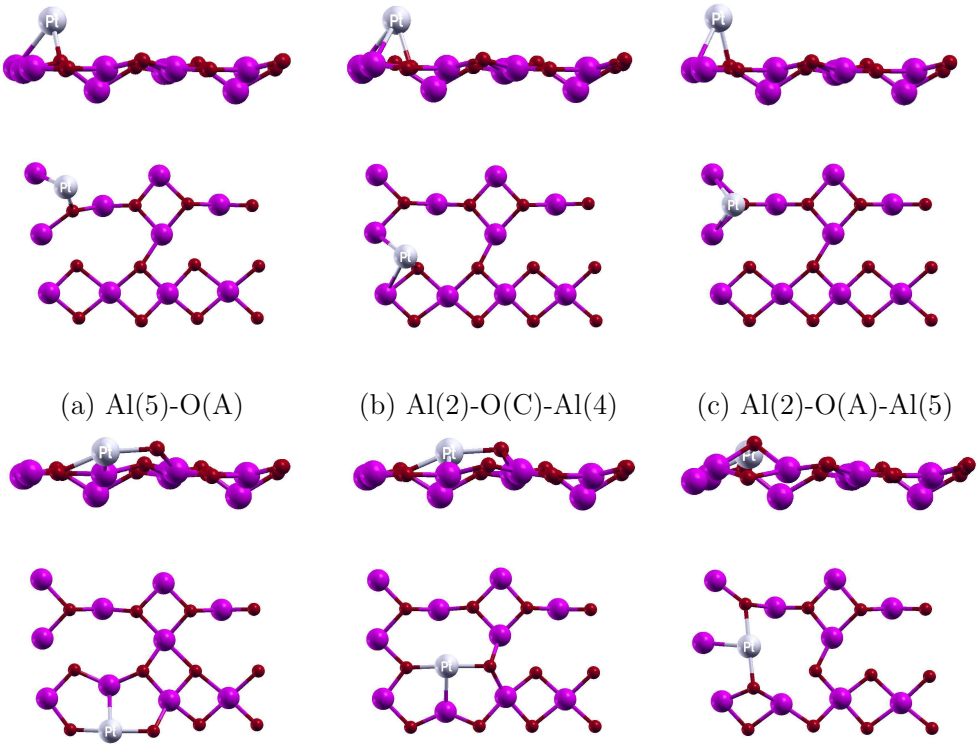

(a) Al(5)-O(A) (b) Al(2)-O(C)-Al(4) (c) Al(2)-O(A)-Al(5)

(d) O(E)-Al(3)-O(F) (e) O(C)-Al(3)-O(D) (f) O(A)-Al(2)-O(C)

Figure 2: Single Pt adsorption sites on γ-Al_2O_3(100) surface. Bridge (a,b), atop (c) and embedded (d,e,f). The numbering scheme is as illustrated in Figure 1.

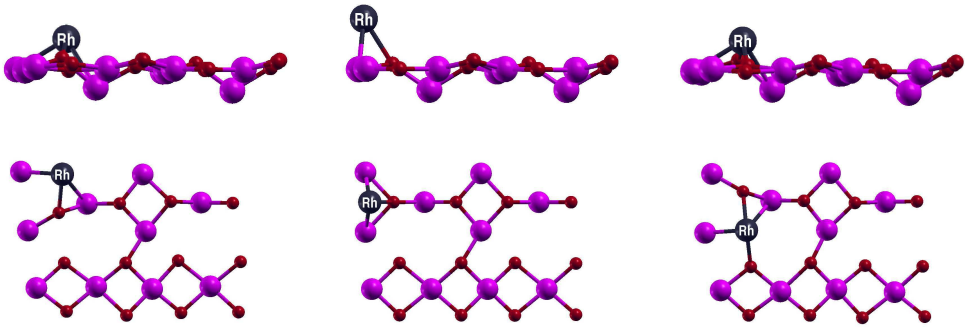

(a) Al(1)-O(A)-Al(5) (b) Al(2)-O(A)-Al(5) (c) O(A)-Al(1)-O(C)-Al(2)

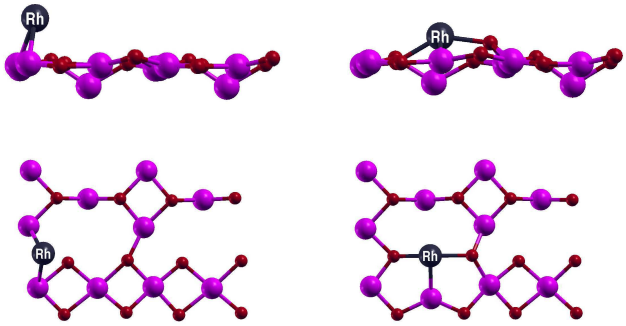

(d) Al(2)-Al(4) (e) O(C)-Al(3)-O(D)

Figure 3: Single Rh adsorption sites on γ-Al_2O_3 (100) surface. Four three-way bridges (a-d) and an embedded configuration (e). The numbering scheme is as illustrated in Figure 1.

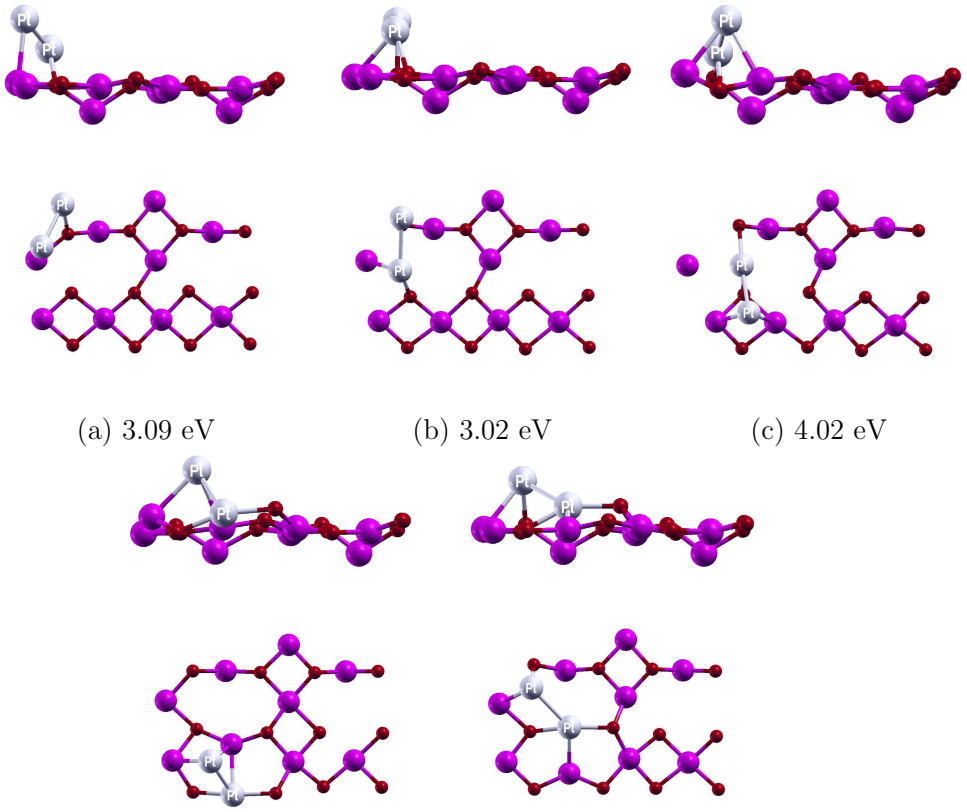

(a) 3.09 eV (b) 3.02 eV (c) 4.02 eV

(d) 2.75 eV (e) 2.28 eV

Figure 4: Pt_2 adsorption geometries on γ-Al_2O_3 (100) surface and binding energies of the second metal atom.

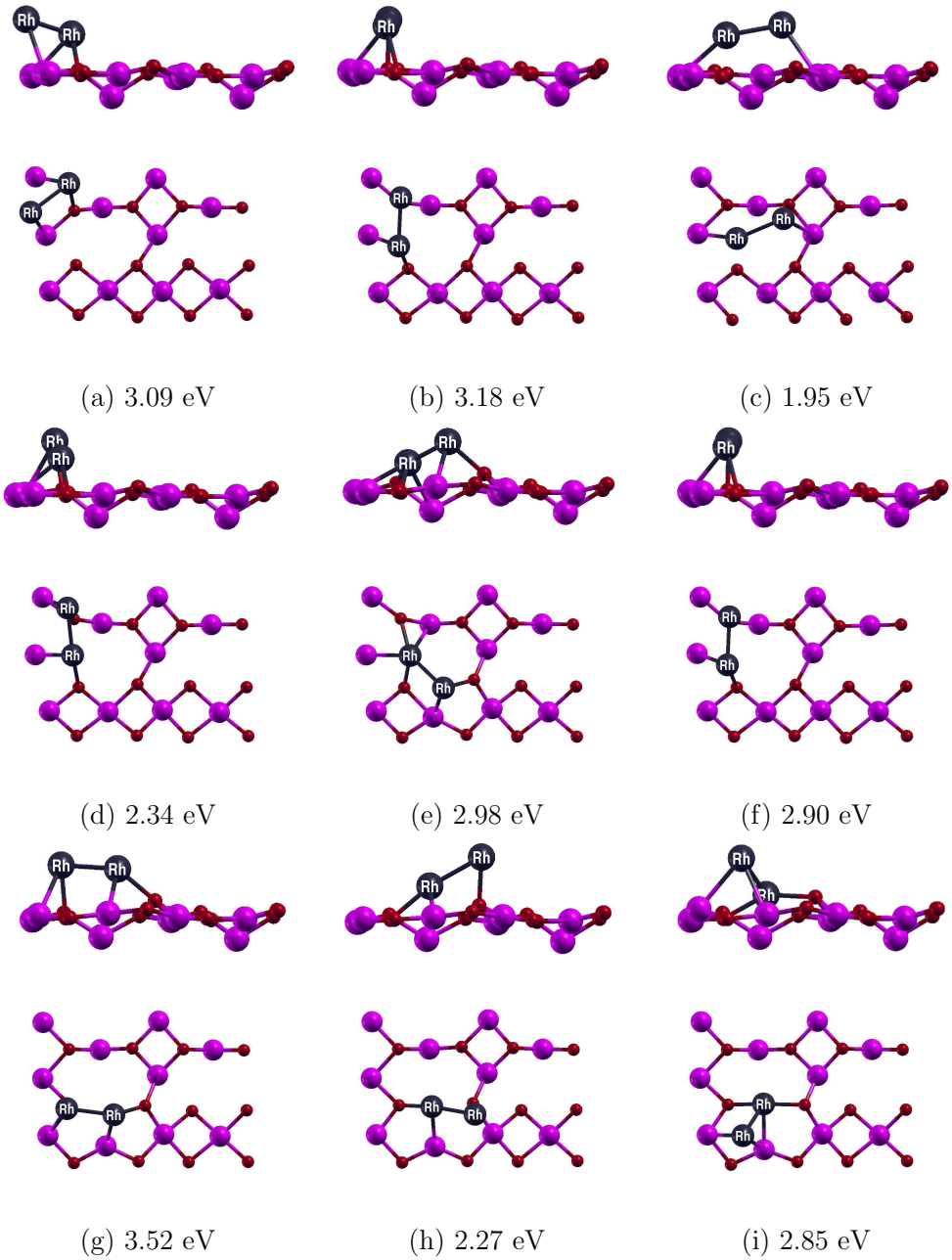

(a) 3.09 eV (b) 3.18 eV (c) 1.95 eV

(d) 2.34 eV (e) 2.98 eV (f) 2.90 eV

(g) 3.52 eV (h) 2.27 eV (i) 2.85 eV

Figure 5: Rh_2 adsorption geometries on γ-Al_2O_3 (100) surface and binding energies of the second metal atom.

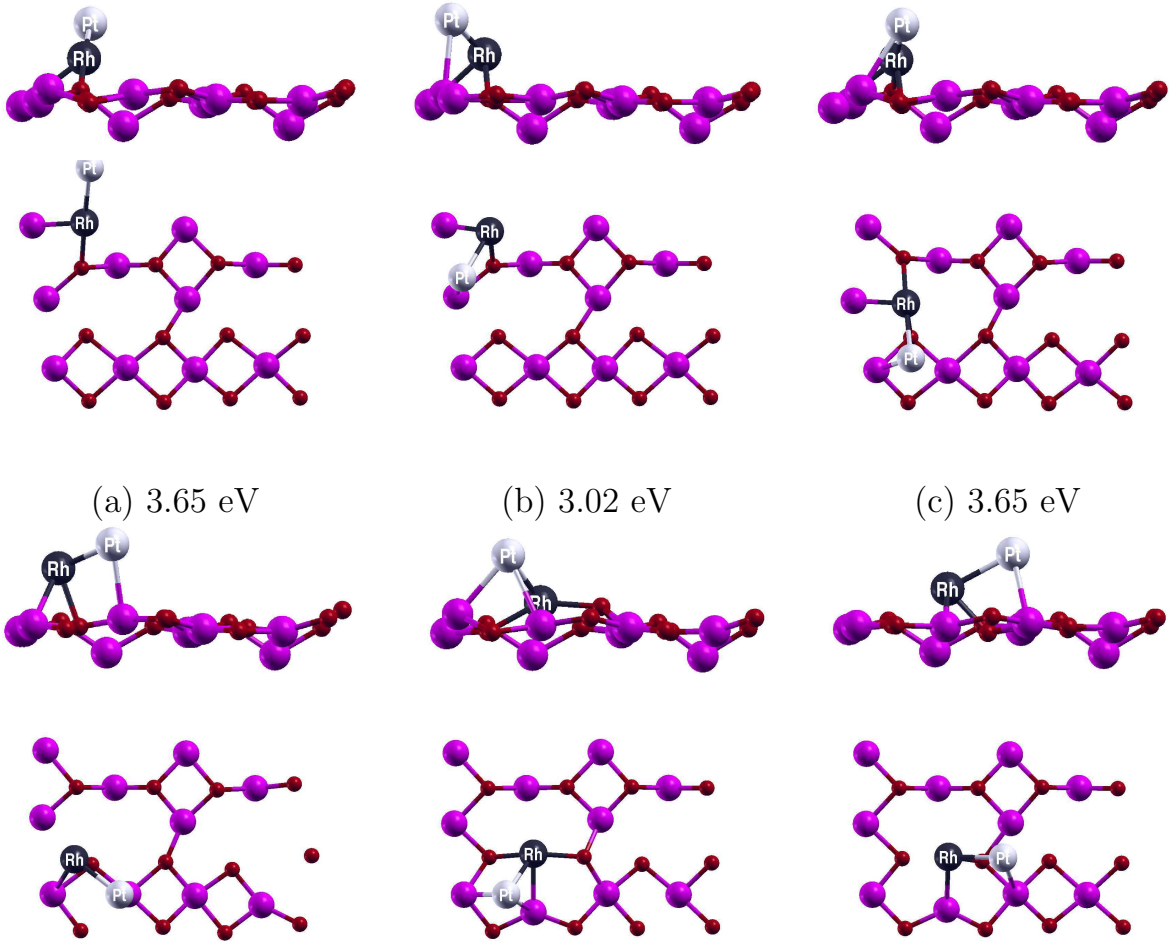

(a) 3.65 eV (b) 3.02 eV (c) 3.65 eV

(d) 3.48 eV (e) 3.48 eV (f) 2.37 eV

Figure 6: PtRh cluster adsorption geometries on γ-Al_2O_3 (100) surface and binding energies of the second metal atom. The Rh atom was preadsorbed on the γ-Al_2O_3 surface.

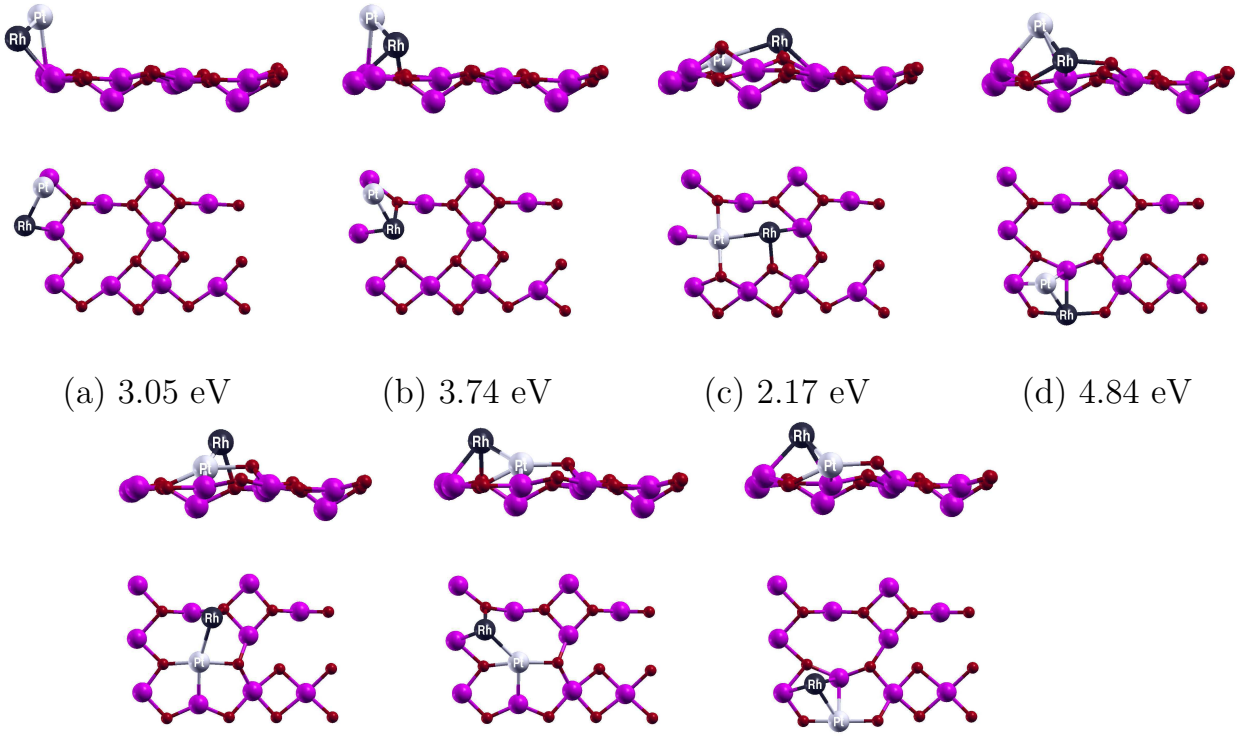

(a) 3.05 eV (b) 3.74 eV (c) 2.17 eV (d) 4.84 eV

(e) 1.62 eV (f) 2.18 eV (g) 2.19 eV

Figure 7: RhPt cluster adsorption geometries on γ-Al_2O_3 (100) surface and binding energies of the second metal atom. The Pt atom was preadsorbed on the γ-Al_2O_3 surface.

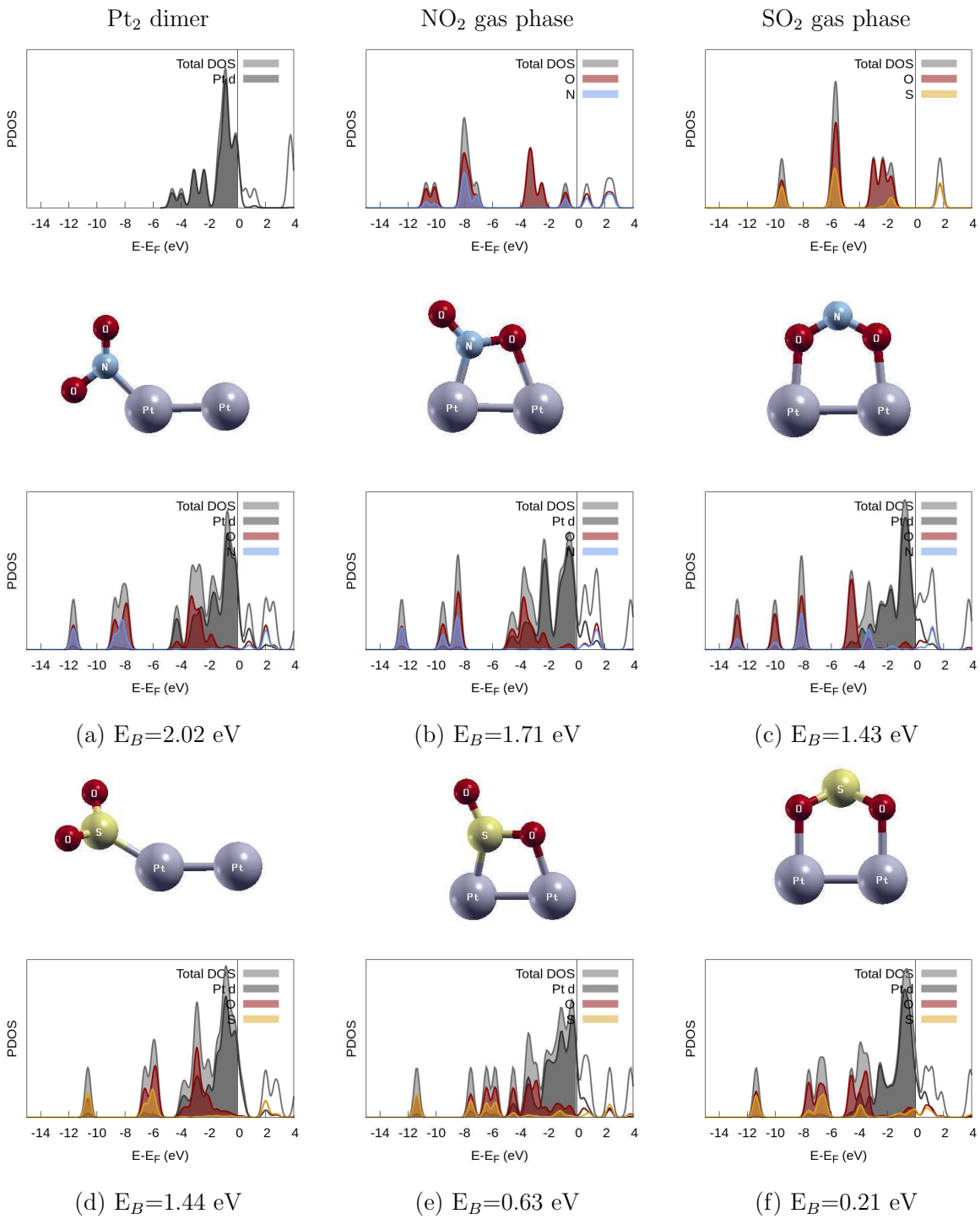

(a) E_B=2.02 eV (b) E_B=1.71 eV (c) E_B=1.43 eV

(d) E_B=1.44 eV (e) E_B=0.63 eV (f) E_B=0.21 eV

Figure 8: Binding geometries and partial density of states (PDOS) of NO_2 and SO_2 molecules on isolated Pt_2 clusters: Monodentate (a and d), N(S)-O bridge (b and e), O-O bridge (c and f).

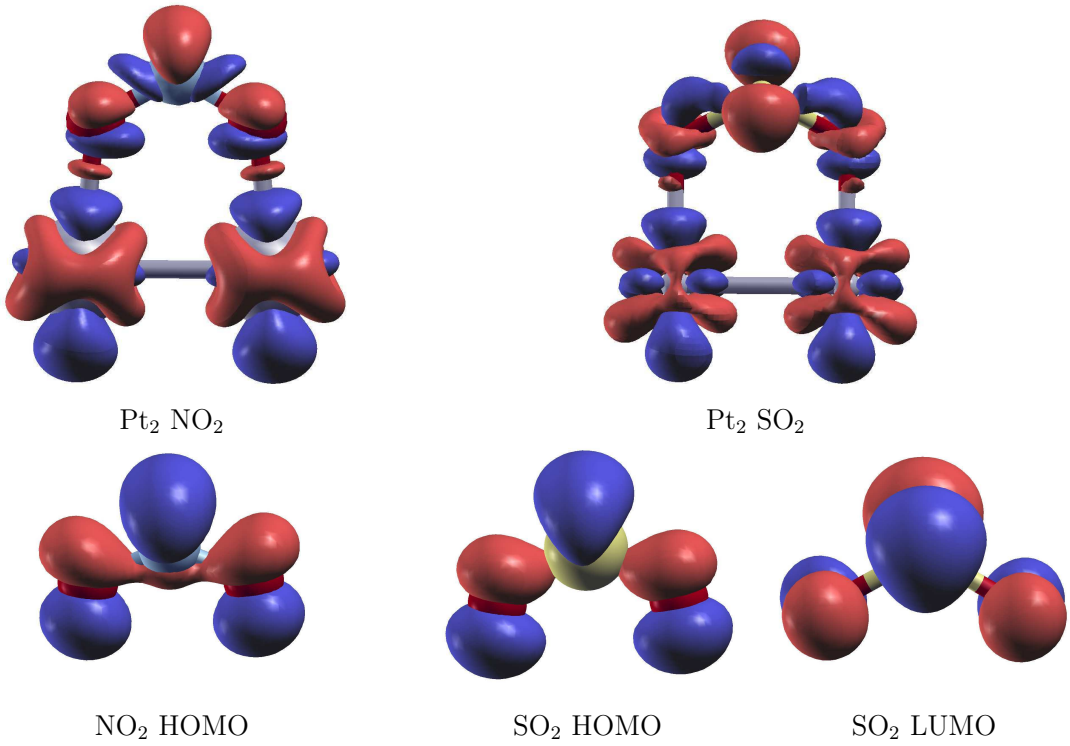

Figure 9: Upper panel: charge density difference plots for NO_2 and SO_2 adsorbed on an isolated Pt_2 cluster (red: electron excess, blue: electron deficiency). Lower panel: HOMO and LUMO probability densities for NO_2 and SO_2. The phase of the molecular orbitals are also plotted.

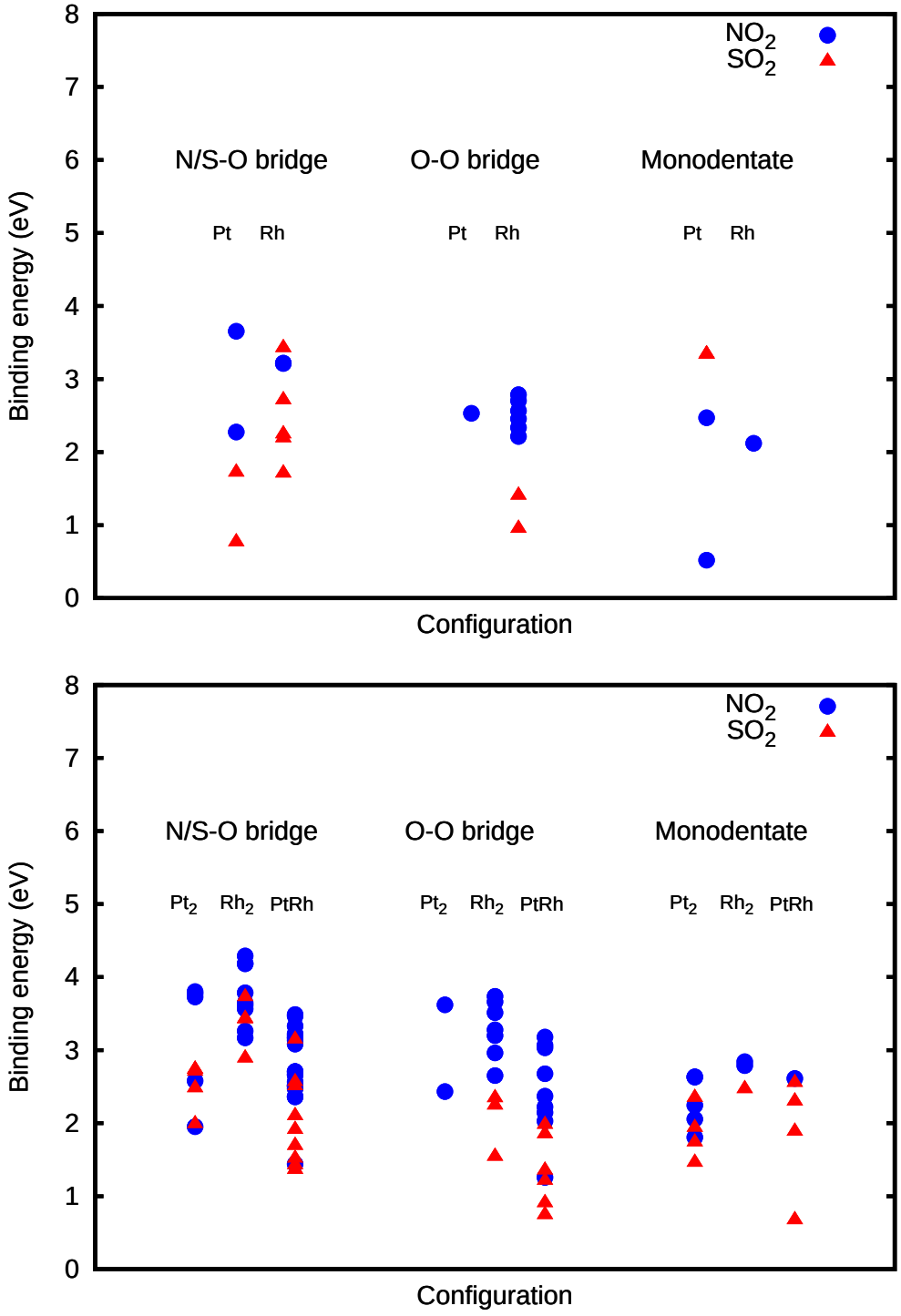

Figure 10: Upper panel: Binding energies of NO_2 and SO_2 on supported mono-atomic clusters. Lower panel: Binding energies of NO_2 and SO_2 on supported diatomic clusters. Adsorption configurations are classified according to Figure 8.

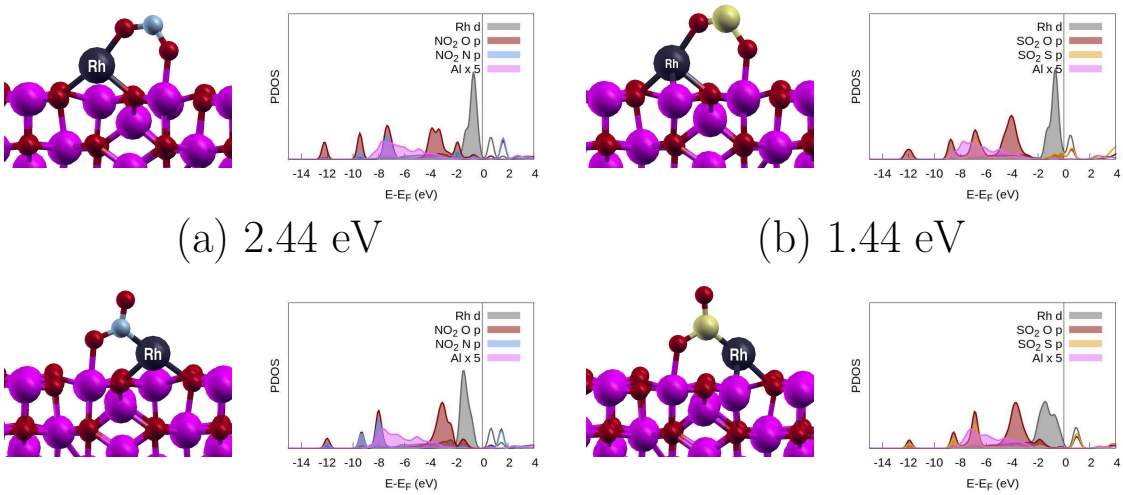

(a) 2.44 eV (b) 1.44 eV

(c) 3.20 eV (d) 2.28 eV

Figure 11: Selected binding geometries for NO_2 and SO_2 adsorption on a supported Rh atom, along with the PDOS analysis.

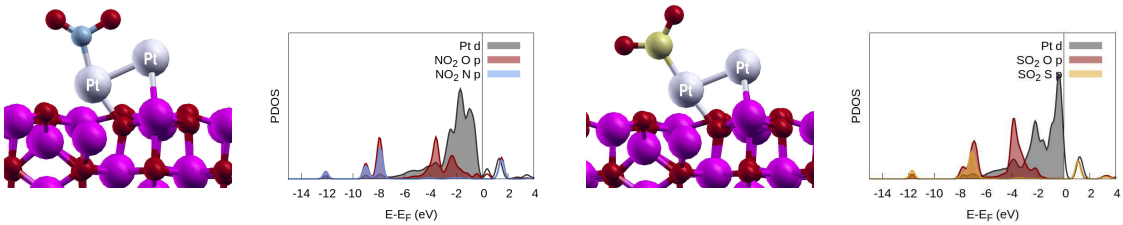

(a) 2.23 (2.02) eV (b) 1.97 (1.44) eV

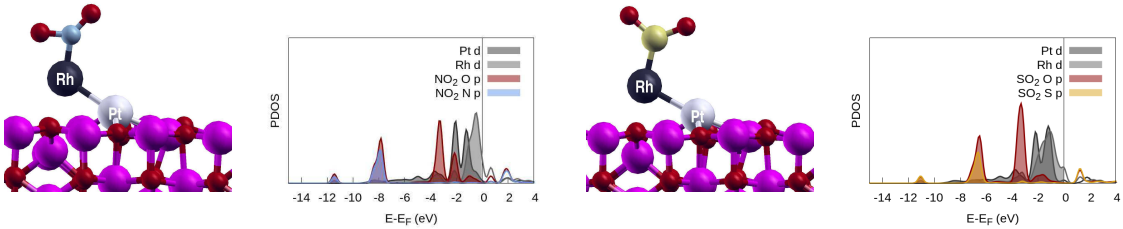

(c) 2.60 (2.05) eV (d) 2.30 (1.19) eV

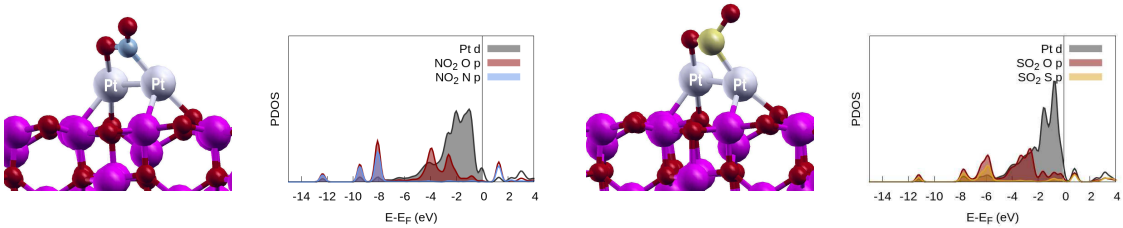

(e) 3.72 (1.71) eV (f) 2.51 (0.63) eV

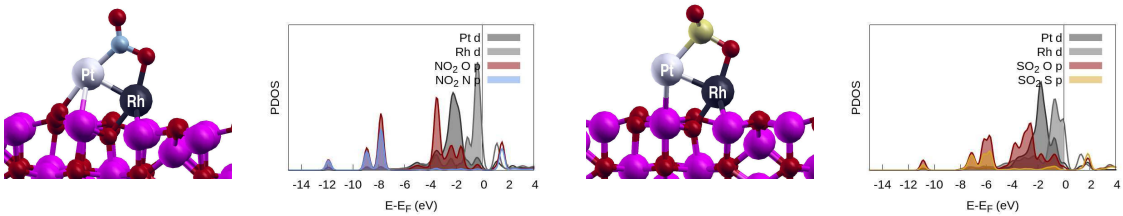

(g) 2.49 (1.92) eV (h) 1.91 (1.66) eV

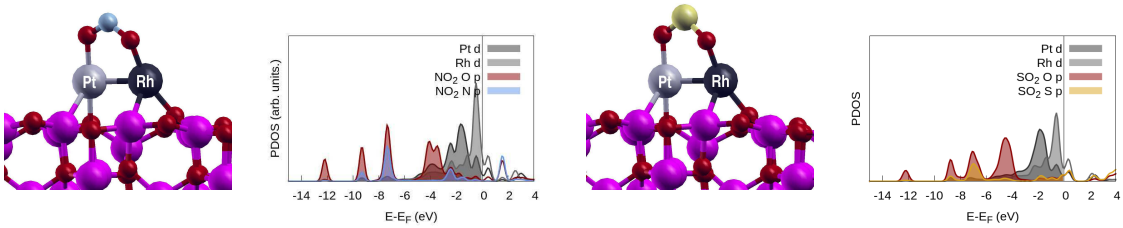

(i) 3.18 (1.64) eV (j) 1.98 (0.48) eV

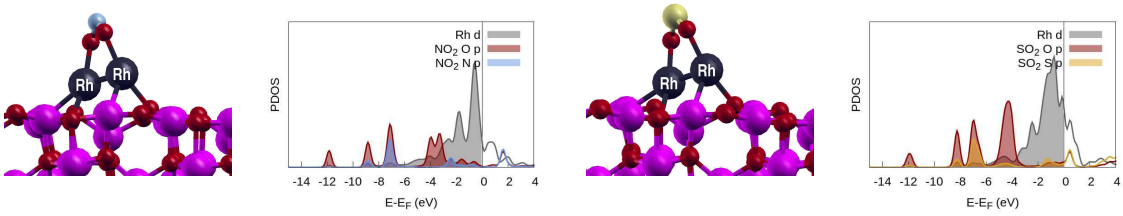

(k) 3.19 (2.17) eV (l) 2.27 (0.91) eV

Figure 12: Selected binding geometries for NO_2 and SO_2 adsorption on supported metal clusters, along with the PDOS analysis. The binding energies in parantheses refer to the corresponding adsorption geometries on isolated clusters.